



Reversible low-temperature redox activity and selective oxidation catalysis derived from concerted activation of multiple metal species on Cr and Rh-incorporated ceria catalysts

Journal:	<i>Physical Chemistry Chemical Physics</i>
Manuscript ID	CP-ART-08-2019-004625
Article Type:	Paper
Date Submitted by the Author:	21-Aug-2019
Complete List of Authors:	Ikemoto, Satoru; Nagoya University, Department of Chemistry Huang, Xiubing; Nagoya University, Research Center for Materials Science Muratsugu, Satoshi; Nagoya University, Department of Chemistry Nagase, Shoko; Nagoya University, Department of Chemistry Koitaya, Takanori; Institute for Molecular Science Matsui, Hirotsuke; Nagoya University, Department of Chemistry Yokota, Gen-ichi; Nagoya University, Department of Chemistry Sudoh, Takatoshi; Nagoya University, Department of Chemistry Hashimoto, Ayako; International Center for Materials Nanoarchitectonics (MANA), Tan, Yuanyuan; Nagoya University, Research Center for Materials Science Yamamoto, Susumu; The Institute for Solid State Physics, The University of Tokyo, Tang, Jiayi; University of Hyogo Matsuda, Iwao; The University of Tokyo, Department of Physics Yoshinobu, Jun; The University of Tokyo Yokoyama, Toshihiko; Institute for Molecular Science, Department of Materials Molecular Science Kusaka, Shinpei; Nagoya University, Department of Chemistry and Biotechnology, School of Engineering Matsuda, Ryotaro; Nagoya University Tada, Mizuki; Nagoya University, Department of Chemistry

ARTICLE

Reversible low-temperature redox activity and selective oxidation catalysis derived from concerted activation of multiple metal species on Cr and Rh-incorporated ceria catalysts

Received 00th January 20xx,
Accepted 00th January 20xx

DOI: 10.1039/x0xx00000x

Satoru Ikemoto,^a Xiubing Huang,^b Satoshi Muratsugu,^{*a,c} Shoko Nagase,^a Takanori Koitaya,^{c,d} Hirotsuke Matsui,^a Gen-ichi Yokota,^a Takatoshi Sudoh,^a Ayako Hashimoto,^{c,e} Yuanyuan Tan,^b Susumu Yamamoto,^f Jiayi Tang,^g Iwao Matsuda,^f Jun Yoshinobu,^f Toshihiko Yokoyama,^d Shinpei Kusaka,^h Ryotaro Matsuda,^h and Mizuki Tada^{*a,b}

The ceria-based catalyst incorporated with Cr and the trace amount of Rh ($\text{Cr}_{0.19}\text{Rh}_{0.06}\text{CeO}_2$) was prepared and the reversible redox performances and its oxidation catalysis of CO and alcohol derivatives with O_2 at low temperatures (< 373 K) were investigated. *In situ* X-ray absorption fine structure (XAFS), ambient-pressure X-ray photoelectron spectroscopy (AP-XPS), high angle annular dark-field scanning transmission electron microscopy (HAADF-STEM)-EDS/EELS and temperature-programmed reduction/oxidation (TPR/TPO) revealed the structures of and redox mechanisms of three metals in $\text{Cr}_{0.19}\text{Rh}_{0.06}\text{CeO}_2$: dispersed Rh^{3+} species (< 1 nm) and $\text{Cr}^{6+}\text{O}_{3-x}$ nanoparticles (~ 1 nm) supported on CeO_2 in $\text{Cr}_{0.19}\text{Rh}_{0.06}\text{CeO}_2$ were transformed to Rh nanoclusters, $\text{Cr}(\text{OH})_3$ species and CeO_{2-x} with two Ce^{3+} -oxide layers at the surface in a concerted activation manner of the three metal species with H_2 .

Introduction

Ceria (CeO_2) is well-known to have an oxygen storage/release capacity (OSC) and a unique property as catalyst support for precious metals, and it has been applied to a wide range of technologies such as automobile exhaust gas-cleaning three-way catalysis, solid oxide fuel cells, solar cells, capacitance and chemical polishing.¹⁻⁴ The OSC of CeO_2 arises from the reversible redox property of Ce between +4 and +3 oxidation states; however, the OSC of pure CeO_2 below 473 K is practically too low, and for the sufficient redox activity high

temperatures above 673 K are usually required.^{3,5}

The addition of zirconia to ceria to form CeZr_xO_y solid solution particularly with an ordered atomic arrangement has been reported to promote OSC tremendously.^{2,3,6-8} The addition of 3d transition metals^{5,9-34} to CeO_2 has been demonstrated to decrease the reduction temperature together with the increase the amount of reducible Ce ions. For examples, $\text{Ce}_{1-x}\text{M}_x\text{O}_{2-y}$ mixed oxides (M = $\text{Cr}^{12,15,23}$, $\text{Mn}^{10,19,23,25,27}$, $\text{Fe}^{14,18,23,27,29,34}$, $\text{Co}^{23,25,27}$, $\text{Ni}^{25,26,27}$, $\text{Cu}^{13,28}$) were reported to exhibit lower reduction temperatures than pure CeO_2 . It has been suggested that the reduction of 3d transition metal ions mainly contributed to the lowest reduction temperature region, and the contribution to Ce reduction was minor. The overall reduction of about 20 to 30% of Ce^{4+} to Ce^{3+} could be achieved on $\text{Ce}_{1-x}\text{Cr}_x\text{O}_{2-y}$,¹² $\text{Ce}_{1-x}\text{Fe}_x\text{O}_{2-y}$,¹⁸ $\text{Ce}_{1-x}\text{Ni}_x\text{O}_{2-y}$,²⁵ CuO/CeO_2 ,²⁴; however, the reduction temperatures were in the range of 777 K and 1073 K, at which Ce^{4+} of the bulk CeO_2 was also reduced. Some systems such as $\text{Ce}_{0.67}\text{Cr}_{0.33}\text{O}_{2-y}$ ¹² and $\text{Ce}_{0.5}\text{Mn}_{0.5}\text{O}_{2-y}$ ¹⁹ were reported to exhibit reversible redox behavior, but other systems such as $\text{Ce}_{0.9}\text{Cu}_{0.1}\text{O}_{2-y}$ ⁷ easily lost its redox activity after reoxidation although it could be reduced at around 383 K.

The addition of noble metals³⁵⁻⁵⁴ to CeO_2 has also been demonstrated to efficiently increase the amount of reducible Ce ions while greatly decreasing their reduction temperatures due to the facile reduction of noble metal ions incorporated in ceria, and the improved redox property has been influenced to its related catalytic activity. Noble metal ion supported/doped ceria systems (Ru/CeO_2 ⁵³, Rh/CeO_2 ^{40,42,44,45,50,51,55}, Pd/CeO_2 ^{42,44,47}, Pt/CeO_2 ^{42,44,54} etc.) and $\text{Ce}_{1-x}\text{M}'_x\text{O}_{2-y}$ mixed

^a Department of Chemistry, Graduate School of Science, Nagoya University. Furo-cho, Chikusa-ku, Nagoya, Aichi 464-8602, Japan.

E-mail: smuratsugu@chem.nagoya-u.ac.jp; Fax: +81-52-788-6093; Tel: +81-52-788-6093

^b Research Center for Materials Science (RCMS) & Integrated Research Consortium on Chemical Science (IRCCS), Nagoya University, Furo-cho, Chikusa-ku, Nagoya, Aichi 464-8602, Japan.

E-mail: mtada@chem.nagoya-u.ac.jp; Fax: +81-52-788-6200; Tel: +81-52-788-6200

^c Japan Science and Technology Agency (JST), Precursory Research for Embryonic Science and Technology (PRESTO), 4-1-8 Honcho, Kawaguchi 332-0012, Japan.

^d Department of Materials Molecular Science, Institute for Molecular Science, Myodaiji-cho, Okazaki, Aichi 444-8585, Japan.

^e In-situ Characterization Technique Development Group, National Institute for Materials Science, 1-2-1 Sengen, Tsukuba 305-0047, Japan.

^f The Institute for Solid State Physics, The University of Tokyo, 5-1-5, Kashiwanoha, Kashiwa, Chiba 277-8581, Japan.

^g Graduate School of Engineering, University of Hyogo, 2167, Shosha, Himeji, Hyogo 671-2280, Japan.

^h Department of Materials Chemistry, Graduate School of Engineering, Nagoya University. Furo-cho, Chikusa-ku, Nagoya, Aichi 464-8602, Japan.

† Electronic Supplementary Information (ESI) available: Characterization and catalytic reaction results of $\text{Cr}_{0.19}\text{Rh}_{0.06}\text{CeO}_2$. See DOI: 10.1039/x0xx00000x

oxides ($M' = \text{Ru}^{41}, \text{Rh}^{39,43,46,52}, \text{Pd}^{46,48}$) exhibited initial reduction of oxidized noble metal ions to zero-valent metal species, and this reduction facilitates the reduction of Ce^{4+} at the similar temperature. For examples, it is reported that the reduction of Rh species in Rh/CeO_2 (1 wt% Rh)⁵⁰ at 373–423 K occurred with the 23% of Ce^{4+} reduction, and the mobile oxygens of CeO_2 determine the oxidation state of Rh species supported on CeO_2 . $\text{Rh}_x\text{Ce}_{1-x}\text{O}_{2-y}$ ($x = 0.05$, Rh: 5.5 wt%) solid solution⁵² exhibited that about 20% reduction of Ce^{4+} species was possible below 423 K together with the reversible redox and morphological change of Rh species ($\text{Rh}^{3+}_x\text{Ce}_{1-x}\text{O}_{2-y} \leftrightarrow \text{Rh}^{\delta+}_n/\text{CeO}_{2-y}$). However, the redox reversibility of some $\text{Ce}_{1-x}\text{M}'_x\text{O}_{2-y}$ mixed oxides were reported to be poor. The reduction of $\text{Ce}_{0.89}\text{Pd}_{0.11}\text{O}_{2-y}$ ⁴⁶ proceeded at 335 K, but it was irreversible. $\text{Ce}_{0.89}\text{Rh}_{0.11}\text{O}_{2-y}$ ⁴⁶ showed a reversible redox activity at 353 K, but the redox was limited to only Rh species and Ce reduction was negligible at the low temperature.

The combination of two or more metal species and CeO_2 has also been investigated to improve the redox property of Ce ions and catalytic activity^{55–75}. On $\text{Pt}/\text{Ce}_{0.75}\text{Zr}_{0.25}\text{O}_2$ ⁵⁸, the ceria reduction reaction with CO proceeded in the kinetically limited regime at 773 K. On Pt/ordered $\text{Ce}_2\text{Zr}_2\text{O}_7$ with remarkable OSC property⁶¹, the supported Pt nanoparticles significantly promoted the reduction of $\text{Ce}_2\text{Zr}_2\text{O}_7$ with H_2 above 573 K. On Pd/ CeO_2 – ZrO_2 – Pr_2O_3 ⁶⁷, the number of oxygen vacancies increased with the increasing Zr, enhancing metal-support interaction and exhibiting better catalytic activity of CO and NO_2 elimination. Ni/ordered $\text{Ce}_2\text{Zr}_2\text{O}_x$ ($x = 7$ – 8) samples catalysed methane steam reforming above 673 K and showed a discontinuity at $x = 7.5$ depending on surface oxygen vacancy and oxygen diffusion efficiency.⁶⁸ CeO_2 -based solid solutions with transition metal ions and noble metal ions^{36,37} (e.g. $\text{Ce}_{0.83}\text{Ti}_{0.15}\text{Pt}_{0.02}\text{O}_{2-y}$ ⁶⁰, $\text{Ce}_{0.89}\text{Fe}_{0.1}\text{Pd}_{0.01}\text{O}_{2-y}$ ⁶³, and $\text{Ce}_{0.88}\text{M}_{0.1}\text{Pd}_{0.02}\text{O}_{2-y}$ ($M = \text{Mn}, \text{Co}, \text{Ni}, \text{Cu}$)⁶⁵) drastically improved the redox performances (temperature, amount of Ce^{4+} species, reproducibility) of solid solutions with only one additional metal ion, and it was suggested that both the reduction of Ce^{4+} and transition metal ions were proceeded after the reduction of noble metal ions. $\text{Ce}_{0.83}\text{Ti}_{0.15}\text{Pt}_{0.02}\text{O}_{2-y}$ ⁶⁰ showed three temperature-programmed reduction (TPR) peaks from 223 K to 393 K (attributed to three redox couples $\text{Pt}^{2+}/\text{Pt}^0$, $\text{Ti}^{4+}/\text{Ti}^{3+}$, and $\text{Ce}^{4+}/\text{Ce}^{3+}$). $\text{Ce}_{0.89}\text{Fe}_{0.1}\text{Pd}_{0.01}\text{O}_{2-y}$ ⁶³ showed a TPR peak at 378 K, and it is suggested that this peak contained not only $\text{Pd}^{2+}/\text{Pd}^0$ redox couples but also $\text{Fe}^{3+}/\text{Fe}^{2+}$ and $\text{Ce}^{4+}/\text{Ce}^{3+}$ redox couples. $\text{Ce}_{0.88}\text{Ni}_{0.1}\text{Pd}_{0.02}\text{O}_{2-y}$ ⁶⁵ exhibited a small TPR peak at around 343 K, but it made little contribution to the overall OSC of the mixed oxide. Thus, it is still difficult to achieve reversible redox performances with the reduction of Ce^{4+} sites below 373 K in addition to the reduction of additional metal species in mixed oxides.

In the present work, we report the structure, reversible low-temperature redox performances, and oxidation catalysis of a new ceria-based catalyst incorporated with Cr and a trace amount of Rh ($\text{Cr}_{0.19}\text{Rh}_{0.06}\text{CeO}_2$). The ceria-based catalyst $\text{Cr}_{0.19}\text{Rh}_{0.06}\text{CeO}_2$ exhibited the remarkable redox activity and unique property due to the concerted contribution of the three metal species to the redox reaction below 373 K. The

reduction of dispersed Rh species, oxidic Cr species and Ce oxide in $\text{Cr}_{0.19}\text{Rh}_{0.06}\text{CeO}_2$ proceeded at the similar temperatures below 373 K, respectively, though their metal oxides are not reduced below 373 K when they exist separately. The redox and catalytic property were characterized by *in situ* X-ray absorption fine structure (XAFS), ambient-pressure X-ray photoelectron spectroscopy (AP-XPS), high angle annular dark-field scanning transmission electron microscopy (HAADF-STEM), X-ray diffraction (XRD), inductively coupled plasma atomic emission spectrometry (ICP-AES), temperature programmed reduction (TPR), and temperature programmed oxidation (TPO).

Results and Discussion

Structure of $\text{Cr}_{0.19}\text{Rh}_{0.06}\text{CeO}_2$

$\text{Cr}_{0.19}\text{Rh}_{0.06}\text{CeO}_2$ was prepared by a hydrothermal method using three metal sources (see Supplementary Information). The compositions of Cr, Rh, and Ce in $\text{Cr}_{0.19}\text{Rh}_{0.06}\text{CeO}_2$ were determined by ICP-AES analysis (Table 1). The surface area of $\text{Cr}_{0.19}\text{Rh}_{0.06}\text{CeO}_2$ was $98 \text{ m}^2 \text{ g}^{-1}$, which was comparable to $118 \text{ m}^2 \text{ g}^{-1}$ for CeO_2 (Table 1). Only the XRD pattern of the fluorite structure of CeO_2 was observed with $\text{Cr}_{0.19}\text{Rh}_{0.06}\text{CeO}_2$, and there was almost no peak shift from the peak pattern of CeO_2 (e.g. 28.9 vs 28.8 $2\theta/^\circ$) as shown in Fig. 1(A), suggesting a negligible effect of added Cr and Rh atoms on the CeO_2 fluorite framework. The transmission electron microscope (TEM) and scanning transmission electron microscope (STEM) images of $\text{Cr}_{0.19}\text{Rh}_{0.06}\text{CeO}_2$ in Figs. 1(C, D) and Fig. S1 revealed clear lattice patterns of CeO_2 fluorite (111) ($d = 0.32 \text{ nm}$). No XRD patterns attributed to Cr oxides (Cr_2O_3 and CrO_3) and metallic and oxidic Rh species (Rh and Rh_2O_3) were observed, indicating no existence of large Cr or Rh particles in the $\text{Cr}_{0.19}\text{Rh}_{0.06}\text{CeO}_2$ sample. HAADF-STEM with energy dispersive X-ray spectroscopy (EDS) provided images of Ce *L* and Rh *L* fluorescent X-rays, and HAADF-STEM with electron energy loss spectroscopy (EELS) provided images of Ce *M* (M_V and M_{IV}) and Cr *L* (L_{III} and L_{II}) as shown in Figs. 1(C, D), S2, and S3, which revealed that both Rh and Cr species were dispersed on the CeO_2 surface. The sizes of supported Rh and Cr species were estimated to be less than 1 nm and to be $\sim 1 \text{ nm}$, respectively.

Cr *K*-edge and Rh *K*-edge X-ray absorption near edge structure (XANES) (Figs. 1(B), S4) and XPS (Fig. 1(E)) clarified the oxidation states of Cr and Rh species in $\text{Cr}_{0.19}\text{Rh}_{0.06}\text{CeO}_2$. The average oxidation states of Cr and Rh in $\text{Cr}_{0.19}\text{Rh}_{0.06}\text{CeO}_2$ were determined to be approximately +5.4 and +3.6, respectively by the edge energy of the XANES spectra. The Cr *K*-edge XANES spectrum was similar to that of CrO_3 , suggesting the formation of Cr^{6+} oxide.^{76,77} In the Cr 2p XPS spectrum (Fig. 1(E-a)), a major peak was observed at 579.7 eV, also suggesting the existence of Cr^{6+} state. Thus, it is most likely from these results that CrO_{3-x} nanoparticles with oxygen defects were formed on the CeO_2 surface.

The Rh 3d_{5/2} XPS peak of $\text{Cr}_{0.19}\text{Rh}_{0.06}\text{CeO}_2$ was observed at 309.4 eV (Fig. 1(E-b)), which was also higher than 308.4 eV of Rh_2O_3 (Rh^{3+})⁸⁰. A similar high-positively charged Rh species on

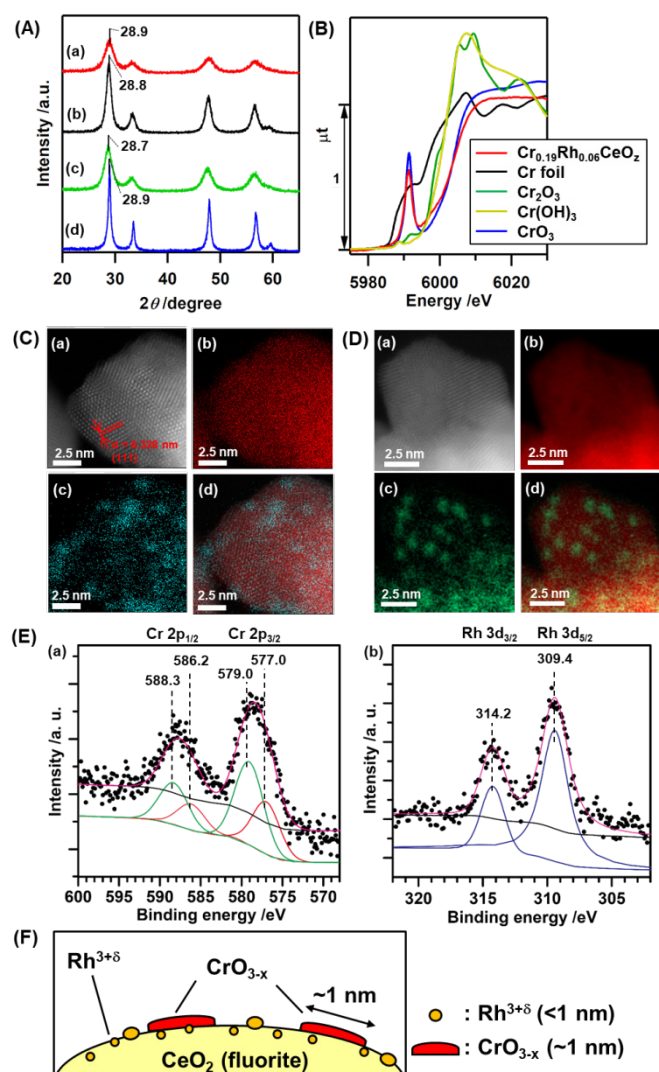


Fig. 1. (A) XRD patterns of (a) $\text{Cr}_{0.19}\text{Rh}_{0.06}\text{CeO}_2$, (b) CeO_2 , (c) $\text{Cr}_{0.17}\text{CeO}_2$, and (d) $\text{Rh}_{0.04}\text{CeO}_2$. (B) Cr K-edge XANES spectra of $\text{Cr}_{0.19}\text{Rh}_{0.06}\text{CeO}_2$ with standard samples. (C) HAADF-STEM-EDS images of $\text{Cr}_{0.19}\text{Rh}_{0.06}\text{CeO}_2$. (a) HAADF-STEM image, (b) EDS mapping of Ce, (c) EDS mapping of Rh, and (d) overlay mapping of Ce and Rh. (D) HAADF-STEM-EELS images of $\text{Cr}_{0.19}\text{Rh}_{0.06}\text{CeO}_2$. (a) HAADF-STEM image, (b) EELS mapping of Ce, (c) EELS mapping of Cr, and (d) overlay mapping of Ce and Cr. (E) (a) Cr 2p and (b) Rh 3d XPS spectra of $\text{Cr}_{0.19}\text{Rh}_{0.06}\text{CeO}_2$. (F) A schematic structural model of $\text{Cr}_{0.19}\text{Rh}_{0.06}\text{CeO}_2$.

ceria has been reported attributed to a high valence Rh species $\text{Rh}^{3+\delta}$ and it was suggested to have a strong interaction with CeO_2 .^{44,46,50,52} Ce valence was attributed to be 4+ from Ce L_{III} -edge XANES⁸¹ (Fig. S4), Ce 3d XPS⁸² (Fig. S5), and EELS analysis. In consequence, the XANES, XPS, and HAADF-STEM-EDS/EELS analysis revealed that the major species of Cr, Rh, and Ce in $\text{Cr}_{0.19}\text{Rh}_{0.06}\text{CeO}_2$ are $\text{Cr}^{6-\gamma}$, $\text{Rh}^{3+\delta}$, and Ce^{4+} (Figs. S4 and S5). Considering the negligible difference in the XRD patterns between $\text{Cr}_{0.19}\text{Rh}_{0.06}\text{CeO}_2$ and CeO_2 , surface sensitivity of the XPS technique, and observed nanodomain structures of Rh and Cr in the STEM-EDS/EELS, a schematic structure of the $\text{Cr}_{0.19}\text{Rh}_{0.06}\text{CeO}_2$ catalyst is proposed in Fig. 1(F), where CrO_{3-x} nanoparticles are supported on fluorite CeO_2 and $\text{Rh}^{3+\delta}$ species are also dispersed with strong interaction with the CeO_2 surface.

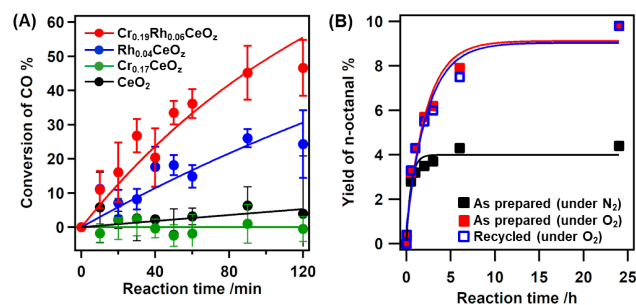


Fig. 2. (A) Reaction profiles of CO oxidation at 363 K. Red: $\text{Cr}_{0.19}\text{Rh}_{0.06}\text{CeO}_2$; blue: $\text{Rh}_{0.04}\text{CeO}_2$; green: $\text{Cr}_{0.17}\text{CeO}_2$; and black: CeO_2 . Reaction conditions: catalyst, 30 mg; CO, 6.0 kPa; O_2 , 3.0 kPa; $\text{Rh}/\text{CO}/\text{O}_2 = 1/50/25$ (molar ratio). Carbon balances were above 0.9. (B) Reaction profiles of 1-octanol oxidation on $\text{Cr}_{0.19}\text{Rh}_{0.06}\text{CeO}_2$ at 343 K. Red: as-prepared catalyst, under O_2 bubbling; black: as-prepared catalyst, under N_2 ; blue: recycled catalyst after calcination, under O_2 bubbling. Reaction conditions: catalyst, $\text{Cr}_{0.19}\text{Rh}_{0.06}\text{CeO}_2$; $\text{Rh}/\text{Cr}/1\text{-octanol}/\text{internal standard (IS)} = 1/3/100/50$, 1-octanol = 0.42 mol L^{-1} ; toluene, 10 mL; IS, dodecane; temperature, 343 K.

Selective oxidation using O_2 at low temperature

It was found that the $\text{Cr}_{0.19}\text{Rh}_{0.06}\text{CeO}_2$ promoted the oxidation of CO at 363 K with a reaction rate of $7.7 \pm 0.6 \text{ mmol g}_{\text{cat}}^{-1} \text{ h}^{-1}$, which was larger than those on $\text{Rh}_{0.04}\text{CeO}_2$ ($3.3 \pm 0.4 \text{ mmol g}_{\text{cat}}^{-1} \text{ h}^{-1}$), $\text{Cr}_{0.17}\text{CeO}_2$ ($\sim 0 \text{ mmol g}_{\text{cat}}^{-1} \text{ h}^{-1}$), and CeO_2 ($\sim 0 \text{ mmol g}_{\text{cat}}^{-1} \text{ h}^{-1}$) as shown in Fig. 2(A). The CO oxidation activities of the oxide catalysts reflect their redox activities (the amount of H_2 consumed and reduction temperatures in TPR of Fig. 3(A), *vide infra*).

The $\text{Cr}_{0.19}\text{Rh}_{0.06}\text{CeO}_2$ catalyst also exhibited a substantial activity for the selective catalytic oxidation of 1-octanol under the atmospheric pressure of O_2 at 343 K (Fig. 2(B)). 1-Octanol was selectively converted to *n*-octanal with the higher selectivity than 99%, and the initial reaction rate ($2.5 \times 10^{-5} \text{ mmol g}_{\text{cat}}^{-1} \text{ min}^{-1}$) was much higher than those of $\text{Rh}_{0.04}\text{CeO}_2$ ($3.2 \times 10^{-6} \text{ mmol g}_{\text{cat}}^{-1} \text{ min}^{-1}$), $\text{Cr}_{0.19}\text{CeO}_2$ ($1.7 \times 10^{-5} \text{ mmol g}_{\text{cat}}^{-1} \text{ min}^{-1}$), and CeO_2 ($\sim 0 \text{ mol g}_{\text{cat}}^{-1} \text{ min}^{-1}$) (Table S1). In the absence of O_2 (under N_2 atmosphere), the oxidation of 1-octanol on $\text{Cr}_{0.19}\text{Rh}_{0.06}\text{CeO}_2$ initially proceeded with a similar reaction rate ($2.1 \times 10^{-5} \text{ mmol g}_{\text{cat}}^{-1} \text{ min}^{-1}$) but stopped after the active oxygen species in $\text{Cr}_{0.19}\text{Rh}_{0.06}\text{CeO}_2$ were consumed as shown in Fig. 2(B). The deactivated $\text{Cr}_{0.19}\text{Rh}_{0.06}\text{CeO}_2$ could be reused as the catalyst with the similar activity ($2.5 \times 10^{-5} \text{ mmol g}_{\text{cat}}^{-1} \text{ min}^{-1}$) after the filtration and calcination at 573 K in air (Fig. 2(B)). These results demonstrate that $\text{Cr}_{0.19}\text{Rh}_{0.06}\text{CeO}_2$ with the low-temperature redox activity acts as an efficient catalyst for the selective oxidation reactions with O_2 at the low temperature. The selective oxidation of benzyl alcohol derivatives was also promoted on the $\text{Cr}_{0.19}\text{Rh}_{0.06}\text{CeO}_2$ catalyst (Table S2).

Low-temperature redox property

It is to be noted that $\text{Cr}_{0.19}\text{Rh}_{0.06}\text{CeO}_2$ exhibited remarkable redox properties at temperatures lower than 373 K (Fig. 3 and Table 1). TPR with H_2 was conducted and the amount of consumed H_2 was estimated. The reduction of $\text{Cr}_{0.19}\text{Rh}_{0.06}\text{CeO}_2$ started at around 308 K and showed a TPR peak at 351 K and 1.96 mmol H_2 per 1 g of $\text{Cr}_{0.19}\text{Rh}_{0.06}\text{CeO}_2$ was consumed in the TPR peak. In contrast, $\text{Cr}_{0.17}\text{CeO}_2$ prepared without the Rh source was reduced at 628 K of a much higher temperature

Table 1. BET surface areas from N₂ adsorption analysis, metal compositions estimated by ICP-AES analysis, and peak top temperatures, consumed H₂ amounts and temperature ranges in TPR for Cr_{0.19}Rh_{0.06}CeO₂ and reference oxides

Prepared oxide	BET surf. area / m ² g ⁻¹	Composition of Cr/Rh/Ce ^a	Peak top temp. /K ^b	Consumed H ₂ /mmol g ⁻¹ (Temp. range /K) ^b
CeO ₂	118	---	673	0.44 (628 ~ 708)
Rh _{0.04} CeO ₂	66	<0.0002 /0.036/1	353	0.55 (308 ~ 423)
Cr _{0.17} CeO ₂	106	0.172 /<0.00049/1	628	1.03 (583 ~ 693)
Cr _{0.19} Rh _{0.06} CeO ₂	98	0.190 /0.063 /1	1 st : 351	1 st : 1.96 ± 0.16 (308 ~ 423)
			2 nd : 351	2 nd : 1.90 ± 0.21 (308 ~ 423)
			3 rd : 351	3 rd : 1.85 ± 0.13 (308 ~ 423)
			4 th : 348	4 th : 1.93 ± 0.18 (308 ~ 423)

^a Determined by ICP-AES. ^b Determined by TPR.

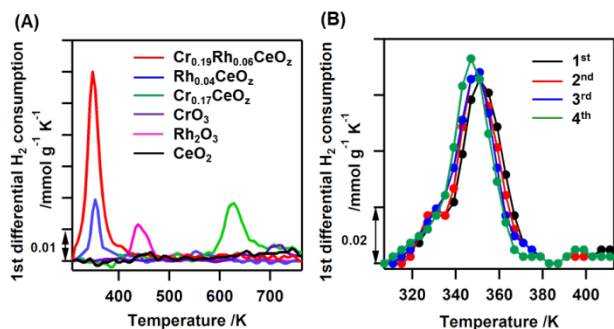


Fig. 3. (A) First differential plots of TPR with H₂ on Cr_{0.19}Rh_{0.06}CeO₂ (red), Cr_{0.17}CeO₂ (green), Rh_{0.04}CeO₂ (blue), CrO₃ (purple), Rh₂O₃ (pink), and CeO₂ (black). (B) First differential TPR plots with H₂ on Cr_{0.19}Rh_{0.06}CeO₂ for four TPR/TPO cycles (black: first cycle; red: second cycle; blue: third cycle; green: fourth cycle). TPO was conducted from 293 to 573 K after TPR up to 423 K.

(Fig. 3(A)). For Rh_{0.04}CeO₂ prepared without the Cr source, the reduction occurred at a similar temperature (353 K), but the amount of H₂ consumed (0.55 mmol g⁻¹) was so small as 28% of the case of Cr_{0.19}Rh_{0.06}CeO₂. Similar low-temperature reductions on Ce_xRh_{1-x}O_{2-y} systems have been reported.^{46,52} CeO₂ exhibited a reduction at 673 K (which can be attributed to surface region of CeO₂)^{13,39,45}, and CrO₃ and Rh₂O₃ were reduced at 628 and 438 K, respectively. These results suggest that the supported Cr and Rh species in Cr_{0.19}Rh_{0.06}CeO₂ dramatically promoted its redox property at the low temperatures (< 373 K).

The reoxidation of a reduced Cr_{0.19}Rh_{0.06}CeO₂ sample after the TPR proceeded readily with O₂ at 303 K, and the amount of O₂ consumed was 0.96 mmol per 1 g of Cr_{0.19}Rh_{0.06}CeO₂, which was comparable to the amount of H₂ consumed. After the reoxidation, the low-temperature reduction proceeded in a similar manner again, and the reversible redox process of Cr_{0.19}Rh_{0.06}CeO₂ was repeated four times. The results of four TPR cycles are shown in Fig. 3(B).

It is reported that there is a contribution of Ce⁴⁺ reduction at the lowered temperature reduction of ceria systems with noble metal ions and 3d transition metal ions.^{36,37,59,61-65,71} To examine the amount of contribution of Ce⁴⁺ ions together with Cr and Rh ions to the redox process, we measured *in situ* Cr *K*-edge, Rh *K*-edge, and Ce *L*_{III}-edge XANES spectra in the reduction process of Cr_{0.19}Rh_{0.06}CeO₂ with H₂ from 293 to 423 K. The *in situ* XANES spectra clearly demonstrated the involvement of all the three metal ions in the reduction process (Figs. 4(A-C)). The Rh *K*-edge XANES spectra firstly changed at the lowest temperature of 332 K, and the average Rh oxidation state changed from +3.6 to +1.4 (Fig. 4(A)). The reduction profile against temperature is shown in Fig. 4(G). Following the reduction of Rh, both Cr *K*-edge and Ce *L*_{III}-edge XANES spectra changed remarkably (Figs. 4(B, C)), which proved the valence decrease in both Cr and Ce ions. The XANES analysis revealed that the average oxidation states of Cr and Ce sites changed from +5.4 to +3.0 (Cr) and from +3.8 to +3.5 (Ce). The reduction-temperature profiles are presented in Fig. 4(G), which shows definite changes in the oxidation states of the Rh, Cr, and Ce ions. The total oxidation state changes in the three metals correspond to 4.59 H mmol g⁻¹, which is comparable to the net consumed H within the experimental error bars in the TPR/TPO and *in situ* XANES. These results demonstrate that the low-temperature reduction of Cr_{0.19}Rh_{0.06}CeO₂ proceeded via the multi-reduction of the three incorporated metals including Ce, not by a single metal source in the material. The temperature gap between Rh and Cr or Ce in the reduction processes (Fig. 4(G)) suggests that the reduced Rh species formed in the first reduction step promote the subsequent reduction of Cr⁶⁺ and Ce⁴⁺ at the CeO₂ surface.

In situ AP-XPS measurements under H₂ revealed the reduced state of Cr_{0.19}Rh_{0.06}CeO₂. A new peak at 307.5 eV appeared in the Rh 3d_{5/2} XPS spectra (Fig. 5(A-a)), which indicates the formation of Rh⁰ species.^{46,52} But the peaks at 309.2 eV (Rh^{3+δ})^{46,52} and 308.4 (attributed to Rh³⁺)^{46,52} remained, which indicates that all Rh ions are not reduced to the metallic level. *In situ* Ce 3d AP-XPS spectra (Fig. 5(B-a)) exhibited the presence of Ce³⁺ (u', v', and v₀ peaks)⁸², and the decrease in the average oxidation state of Ce to +3.5 indicates that Ce⁴⁺ ions in Cr_{0.19}Rh_{0.06}CeO₂ was partially reduced. The *in situ* Cr 2p_{3/2} AP-XPS peak shifted from 579.1 to 577.0 eV, indicating the formation of Cr³⁺ species (Fig. 5(C-a))^{12,78,79}, which agreed with the results of Cr *K*-edge XANES (Fig. 4(B)). The shape of the Cr *K*-edge XANES spectrum after the reduction was similar to that of Cr(OH)₃ (Figs. 4(B) and Fig. S4(A)), suggesting the formation of Cr(OH)₃ below 373 K. The appearance of a new peak at 531.6 eV in the *in situ* O 1s AP-XPS also suggested the formation of Cr(OH)₃ after the reduction (Fig. 5(D-a)).⁷⁸

The *in situ* XANES spectra for the reoxidation process (Figs. 4(D-F)) also revealed the oxidation states of Rh, Cr, and Ce in Cr_{0.19}Rh_{0.06}CeO₂ (Fig. 4(H)). Note that the oxidation process rapidly proceeded on Rh and Ce at 303 K; however, the oxidation event on Cr gradually proceeded from 350 to 550 K. It was found that the oxidation started at temperatures lower than 273 K. The increases in the oxidation states of Rh, Cr, and Ce were reversible as shown in Figs. 4(G, H). *In situ* AP-XPS

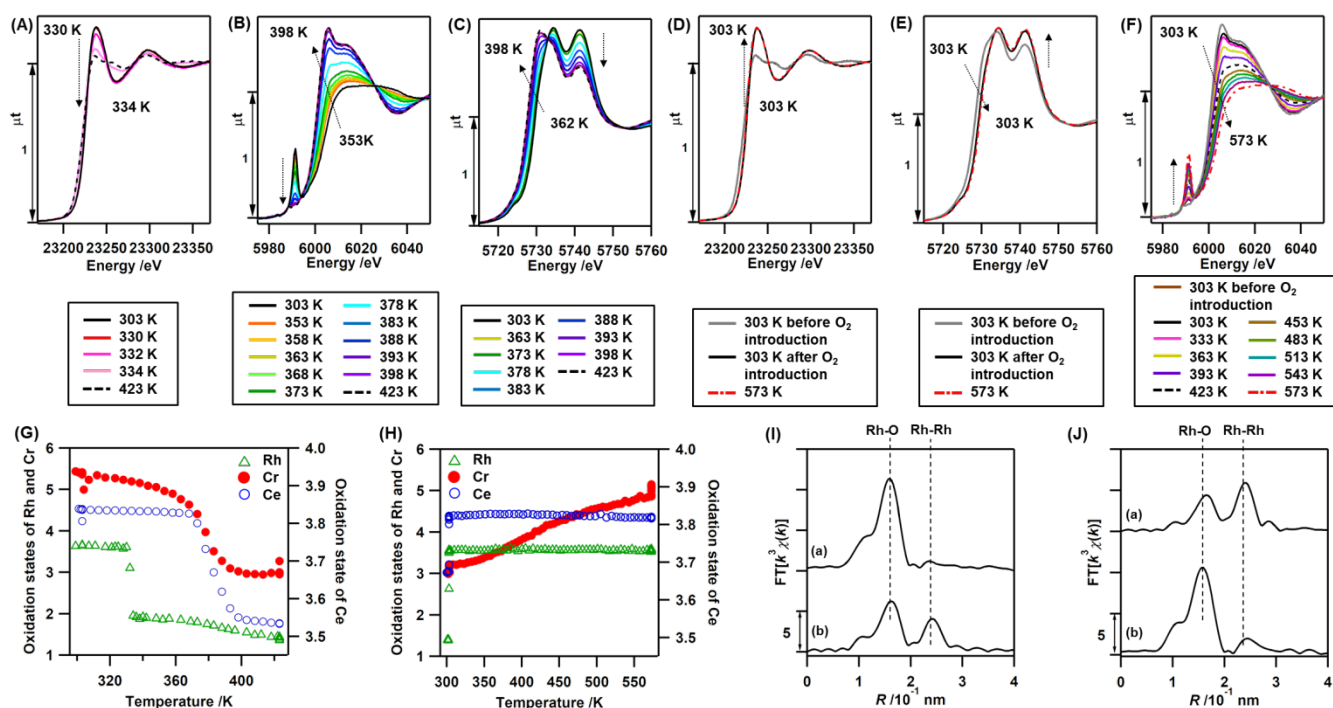


Fig. 4. *In situ* (A) Rh *K*-edge, (B) Cr *K*-edge, and (C) Ce *L*_{III}-edge XANES spectra for the reduction with H₂ from 303 to 423 K. Black solid line: before the reduction at 303 K; black dashed line: at 423 K under H₂. *In situ* (D) Rh *K*-edge, (E) Ce *L*_{III}-edge, and (F) Cr *K*-edge XANES spectra of Cr_{0.19}Rh_{0.06}CeO₂ under O₂ oxidation conditions (303–573 K, 573 K for 1 h). Black solid line: before O₂ oxidation at 303 K, black dashed line: at 573 K (1 h heating) under O₂. (G) Changes in the oxidation states of Rh (green), Cr (red), and Ce (blue) estimated from the XANES spectra for the reduction process. (H) Changes in the oxidation states of Rh (green), Cr (red), and Ce (blue) estimated from the XANES spectra for the oxidation process. (I) *k*³-weighted Rh *K*-edge Fourier transforms (*k* = 30–140 nm⁻¹) for Cr_{0.19}Rh_{0.06}CeO₂ (a) during H₂ reduction at 330 K and (b) during H₂ reduction at 334 K. (J) *k*³-weighted Rh *K*-edge Fourier transforms (*k* = 30–140 nm⁻¹) for Cr_{0.19}Rh_{0.06}CeO₂ (a) before O₂ oxidation at 303 K and (b) after O₂ oxidation at 303 K.

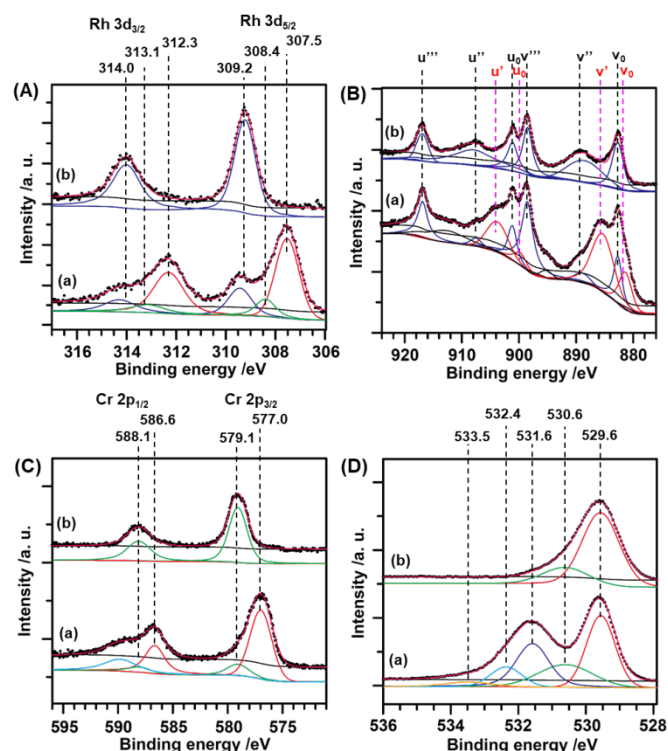


Fig. 5. *In situ* (A) Rh 3d, (B) Ce 3d, (C) Cr 2p, and (D) O 1s AP-XPS spectra of Cr_{0.19}Rh_{0.06}CeO₂. (a) measured under H₂ reduction at 385 K, (b) measured under O₂ oxidation at 573 K.

spectra also supported reversible changes in the oxidation states of Rh, Cr, and Ce at the reoxidation process (Fig. 5(A, B, C-b)). The gradual oxidation of Cr might be caused by the oxidation of hydroxyl species accompanied with the desorption of H₂O. The Ce valence change (30–40% of Ce; estimated by Ce *L*_{III}-edge XANES and Ce 3d AP-XPS) during the redox processes corresponded to approximately two monolayers of Ce species on the most stable (111) surface of CeO₂^{83,84}, taking into account the surface area of 98 m² g⁻¹ and an average particle size of 10 nm from the STEM image.

Rh firstly reacted in the both reduction and oxidation processes and it may be crucial in the low-temperature redox properties of Cr_{0.19}Rh_{0.06}CeO₂. We investigated the local coordination structure of the Rh species by *in situ* Rh *K*-edge extended X-ray absorption fine structure (EXAFS) analysis (Figs. 4(I, J), Fig. S6, and Table S3). Before the reduction, there were Rh-O bonds at 0.204 ± 0.001 nm (coordination number (CN) = 5.8 ± 1.3), and the Rh-Rh bonds of metallic Rh and the Rh-O-Rh bonds in Rh₂O₃ were not detected (Fig. 4(I-a)). After the reduction, Rh-Rh bonds at 0.270 ± 0.002 nm (CN = 2.6 ± 0.7) were observed in addition to the Rh-O bond at 0.205 ± 0.002 nm (Fig. 4(I-b)). The local Rh coordination structure recovered after the reoxidation process (Figs. 4(J), S6, and Table S3). Thus, it is concluded that the reversible structural transformations between dispersed Rh^{3+δ} species and small Rh nanoclusters occur during the redox processes of Cr_{0.19}Rh_{0.06}CeO₂.

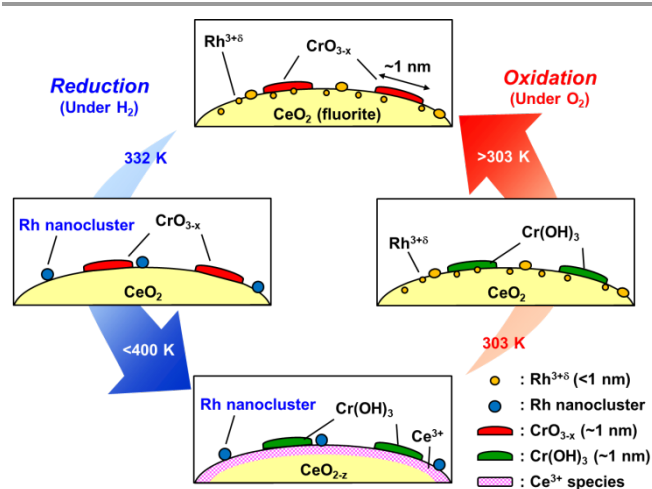


Fig. 6. Schematic of the structural changes in the reversible low-temperature redox process of $\text{Cr}_{0.19}\text{Rh}_{0.06}\text{CeO}_z$ under H_2 or O_2 based on *in situ* surface structural and electronic characterizations.

Based on the results of the *in situ* characterization of $\text{Cr}_{0.19}\text{Rh}_{0.06}\text{CeO}_z$, the structures and reversible low-temperature redox mechanism of $\text{Cr}_{0.19}\text{Rh}_{0.06}\text{CeO}_z$ are proposed as follows (Fig. 6).

(1) Initial structure of $\text{Cr}_{0.19}\text{Rh}_{0.06}\text{CeO}_z$: $\text{Rh}^{3+\delta}$ ions were dispersed and interacted with the surface layers of CeO_2 fluorite, and small CrO_{3-x} ($\text{Cr}^{6-\gamma}$) nanoparticles (~ 1 nm) were distributed on CeO_2 .

(2) Low-temperature reduction with H_2 : the $\text{Rh}^{3+\delta}$ species were firstly reduced and clusterized at 332 K. Then, the dual reduction of Cr and Ce was promoted at around 360 K: $\text{Cr}^{6-\gamma}$ (CrO_{3-x}) was converted to $\text{Cr}^{3+}(\text{OH})_3$ and Ce^{4+} species at the surface layers of CeO_2 was reduced to Ce^{3+} .

(3) Reversible reoxidation with O_2 : The concerted oxidation of the Rh nanoclusters and surface/subsurface Ce^{3+} species proceeded immediately after O_2 introduction below 303 K. Then, the remaining Cr^{3+} species gradually reverted to $\text{Cr}^{6-\gamma}$ at 303–573 K.

Similar reversible structural change of Rh species was also reported on $\text{Rh}_{0.05}\text{Ce}_{0.95}\text{O}_{2-y}$ solid solution ($\text{Rh}^{3+}_x\text{Ce}_{1-x}\text{O}_{2-y} \leftrightarrow \text{Rh}_n^{\text{dt}}/\text{CeO}_{2-y}$)⁵². The overall redox performances of $\text{Cr}_{0.19}\text{Rh}_{0.06}\text{CeO}_z$ is similarly interpreted that the structural transformation of the dispersed Rh species strongly interacted on the CeO_2 surface can decrease the redox temperatures of both CrO_{3-x} and Ce^{4+} at the surface layers at the similar value below 373 K.

Conclusions

In summary, the ceria-based catalyst incorporated with Cr and the trace amount of Rh ($\text{Cr}_{0.19}\text{Rh}_{0.06}\text{CeO}_z$) was found to show the remarkable and reversible low-temperature redox activity at < 373 K. Not only Cr and Rh but also Ce contributed to the low-temperature redox process of the $\text{Cr}_{0.19}\text{Rh}_{0.06}\text{CeO}_z$ as characterized by *in situ* XAFS, *in situ* AP-XPS, HAADF-STEM-EDS/EELS and TPR/TPO. The advanced physical techniques also revealed dispersed $\text{Rh}^{3+\delta}$ species (< 1 nm) and $\text{Cr}^{6-\gamma}\text{O}_{3-x}$ nanoparticles (~ 1 nm) supported on CeO_2 . The $\text{Rh}^{3+\delta}$, $\text{Cr}^{6-\gamma}\text{O}_{3-x}$,

and CeO_2 in $\text{Cr}_{0.19}\text{Rh}_{0.06}\text{CeO}_z$ were transformed to Rh nanoclusters, $\text{Cr}(\text{OH})_3$ species and CeO_{2-x} with two Ce^{3+} -oxide layers at the surface in a concerted activation manner of the three metal species with H_2 . The low-temperature redox property was also found to bring about the efficient catalysis for selective oxidation reactions of CO, 1-octanol and benzyl alcohol derivatives with O_2 below 373 K.

Experimental Section

Preparation of ceria-based catalysts

Chemicals were purchased from commercial sources and used without further purification unless noted. A typical preparation process for $\text{Cr}_{0.19}\text{Rh}_{0.06}\text{CeO}_z$ was as follows. $\text{Ce}(\text{NO}_3)_3 \cdot 6\text{H}_2\text{O}$ (3.5 mmol; Sigma-Aldrich, 99.99%), $\text{Cr}(\text{NO}_3)_3 \cdot 9\text{H}_2\text{O}$ (0.67 mmol; Sigma-Aldrich, 99%), and $\text{RhCl}_3 \cdot 3\text{H}_2\text{O}$ (0.22 mmol; Wako, 99.5%) were dissolved in deionized water (18 mL) under continuous stirring. A 7 M aqueous NaOH solution (53 mL) was added to the mixture. After stirring for 30 min, the slurry was transferred to a Teflon-lined stainless steel vessel autoclave with a volume of 100 mL. The autoclave was sealed and kept in an electric oven at 373 K for 24 h. After cooling to room temperature, the precipitate was separated by centrifugation, washed with deionized water and ethanol several times, and dried in air at 353 K for 12 h. The powder was ground and calcined at 573 K for 2 h. $\text{Cr}_{0.17}\text{CeO}_z$ and $\text{Rh}_{0.04}\text{CeO}_z$, respectively, were prepared by this method without the Rh and Cr precursors. CeO_2 was also prepared by this method without the Cr and Rh precursors.

Characterization

The atomic compositions of samples were analyzed by ICP-AES (Vista-Pro-AX, Varian). Oxide samples were treated with fuming nitric acid at 353 K until solids were completely dissolved, and the solutions were diluted with distilled water for analysis. Nitrogen adsorption was performed on a surface adsorption analyzer (Micromeritics ASAP-2020, Shimadzu) at 77 K. XRD patterns were recorded on an X-ray diffractometer (MultiFlex, Rigaku) at 293–298 K under air. TEM and HAADF-STEM images with EDS and EELS spectra were taken using a transmission electron microscope (JEM-ARM 200F, JEOL, High Voltage Electron Microscope Laboratory, Institute of Materials and Systems for Sustainability, Nagoya University, Japan; accelerating voltage of 200 kV). XPS was performed on X-ray photoelectron spectrometers: (ECSA3057, ULVAC PHI and R4000, Scienta Omicron). The binding energies were referenced to the O 1s peak of CeO_2 lattice oxygen (529.6 eV). XAFS spectra at the Cr K-edge and Ce L_{III}-edge were measured at the BL9C and BL12C stations, and XAFS spectra at the Rh K-edge were measured at the NW10A station of the Photon Factory at KEK-IMSS (Tsukuba, Japan). All samples were measured in transmission mode at 298 K. The XAFS spectra were analyzed using ATHENA and ARTEMIS with IFFFIT (version 1.2.11).^{85,86} The threshold energy was tentatively set at the inflection point for the Cr K-edge (Cr foil: 5988.8 eV)⁸⁷ and Rh K-edge (Rh foil: 23219.8 eV),⁸⁷ and at the first peak top

of the white line for the Ce L_{III} -edge (CeO₂: 5734.4 eV), and the background was subtracted by the Autobk method.^{88,89} The average oxidation states of Ce, Cr, and Rh were determined from the changes at 5741.3 eV (second peak top of the white line), 5991.4 eV (pre-edge), and 23,218 eV (white line peak top), respectively. The k^3 -weighted extended XAFS (EXAFS) oscillations were Fourier transformed into R -space. Curve-fitting analysis was carried out in the R -space. Detailed characterization analyses are presented in ESI.

TPR/TPO measurements

TPR and TPO were carried out in a closed glass reactor (Fig. S7) with a gas circulation unit and pressure gauge. Typically, the sample (200 mg) was evacuated in a reactor for 30 min, H₂ was introduced into the reactor, and the temperature was increased to the target temperatures (4 or 5 K min⁻¹). H₂O formed during the TPR was trapped by a liquid N₂ trap. Changes in the system pressure were recorded at appropriate intervals. TPO was performed after the TPR processes. Oxygen was put into the reactor at 293 K. Then, the system was heated to 573 K (5 K min⁻¹) and kept at 573 K for 1 h. Finally, the system was cooled to 293 K and changes in the pressure of the system were measured to estimate the oxygen consumption. Desorbed H₂O was trapped by a dry-ice/acetone trap during the TPO.

In situ XAFS measurements

In situ quick XAFS (QXAFS) measurements during reduction with H₂ or oxidation with O₂ conditions were performed at the Photon Factory at KEK-IMSS as follows. A sample was pelletized into a disk and placed in an *in situ* XAFS cell placed in an experimental setup as shown in Fig. S8. After flushing with N₂ (100 sccm) for 10 min, the cell was heated to 303 K and kept at this temperature for 5 min. Then, the QXAFS measurement was started. The protocols are shown in Scheme S1, and the energy range, scan time, and scan interval are listed in Table S4. After 5 min, the gas was changed to H₂ + N₂ (50 + 50 sccm) and the temperature was held for another 5 min. Then, the cell was heated to 423 K at a rate of 2 K min⁻¹. After keeping the temperature at 423 K for 10 min, the gas was changed to N₂ (100 sccm), and the cell was cooled to room temperature. The cell was heated again to 303 K and kept at this temperature for 5 min, and the QXAFS measurement was started. After 5 min, the gas was changed to O₂ + N₂ (50 + 50 sccm) and the temperature was held for another 5 min. Then, the cell was heated to 573 K at a rate of 5 K min⁻¹. After keeping the temperature at 573 K for 1 h, the gas was changed to N₂ (100 sccm), and the cell was cooled to room temperature.

In situ AP-XPS measurements

AP-XPS measurements under H₂ reduction and O₂ oxidation conditions were performed at the soft X-ray undulator beamline BL07LSU of SPring-8 (Harima, Japan). In the reduction (oxidation) experiments, the sample was exposed to 130 Pa H₂ gas (200 Pa O₂ gas) at room temperature, followed by heating to 385 K (573 K), respectively. O 1s, Cr 2p, and Rh 3d measurements under ambient conditions were conducted

at a photon energy of 760 eV, whereas the Ce 3d spectra were collected at a photon energy of 1070 eV. A slight peak shift to higher binding energy was observed under the H₂ reduction conditions due to sample charging, and the binding energy was referenced to the O 1s peak of CeO₂ lattice oxygen (529.6 eV). The binding energies of the AP-XPS spectra measured under oxidation conditions at 573 K were referenced to the Fermi edge of Au foil. The spectra were fitted by Voigt functions after Shirley background subtraction.

Catalytic Reactions

Catalytic CO oxidation: CO oxidation was carried out in a closed glass reactor (Fig. S9) with a gas circulation unit and pressure gauge equipped with a gas chromatograph with a thermal conductivity detector (TCD; GC-8, Shimadzu) and a SHINCARBON-ST column (Shimadzu; 3 mm (I.D.) × 2 m). Typically, the sample (30 mg) was evacuated in a reactor for 30 min. CO and O₂ were mixed well with a circulation unit for more than 30 min, and small portion of the gases was introduced to a glass loop and analyzed by the TCD (defined as 0 min). The reactor temperature was increased to the target temperatures (353, 363, and 373 K; 2 K min⁻¹), and held for 30 min. Then, the mixed gas was circulated in the reactor, and the gases were analyzed at appropriate intervals. The initial pressures of CO and O₂ at 0 min were 6.0 and 3.0 kPa, respectively, and the molar ratio of Rh/CO/O₂ was 1/50/25. Carbon balances were above 0.9.

Catalytic oxidation of alcohol: A three-necked flask with a Cr_{0.19}Rh_{0.06}CeO₂ (150 mg) was connected to a reflux condenser and heated at 343 K, and the atmosphere of the reactor was exchanged to 101.3 kPa of O₂. The preheated mixture of alcohol (4.75 mmol, 0.42 M), dodecane (internal standard, 2.38 mmol), and dry toluene (10 mL) was added to the reactor. The molar ratio of Rh/Cr/alcohol/dodecane was 1/3/100/50. O₂ was fed through a toluene trap and bubbled through the reaction solution and the reaction mixture was stirred. The reaction mixture was analyzed at appropriate intervals by FID-GC (GC-2014s, Shimadzu) and GC-MS (GC-2010, PARVUM2, Shimadzu) with an InertCap 5 column (GL Science; 0.25 μm (df) × 0.25 mm (I.D.) × 30 m). The reaction under N₂ was performed in a Schlenk tube with a balloon filled with N₂.

Catalyst recycling test: The scale of catalytic oxidation of alcohol was doubled for this experiment. The recycling of the oxide catalyst was performed by filtering the solid catalyst after 24 h. The reaction solution was transferred to a 15 mL Eppendorf tube under a nitrogen flow and the catalyst was precipitated by centrifugation. The supernatant was removed, and the catalyst was washed with toluene and centrifuged again. After the catalyst was cleaned in this manner three times, it was evacuated over half a day and dried (filtered catalyst). The dried catalyst was calcined at 573 K for 2 h in air (calcined catalyst). The recycling oxidation was carried out using both the filtered and the calcined catalysts.

Conflicts of interest

There are no conflicts to declare.

Acknowledgements

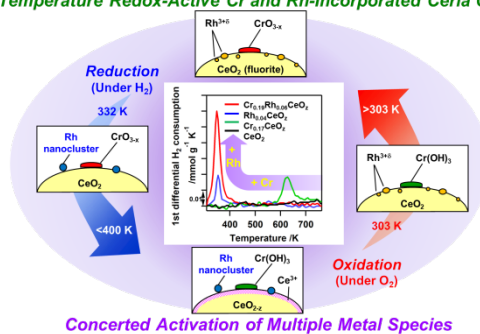
The work was financially supported in part by JSPS KAKENHI Grant Nos. (26288005, 18K05144, 18H01940, 17K14432), the JST PRESTO program (No. 15665997), the JST ACT-C project (No. JPMJCR12YU), the Integrated Research Consortium on Chemical Sciences, the Sumitomo Foundation, and the Tokuyama Foundation. XAFS measurements were performed with the approval of PF-PAC (Nos. 2016G093 and 2017G534). XPS measurements were partially conducted at the Nagoya University Nanofabrication Platform, supported by the "Nanotechnology Platform Program" of MEXT, Japan. HAADF-STEM-EDS/EELS measurements were conducted at the High Voltage Electron Microscope Laboratory, IMSS, Nagoya University, supported by the "Advanced Characterization Nanotechnology Platform" of MEXT, Japan. We thank Mr. K. Higuchi (Nagoya University) for HAADF-STEM measurements. We thank Dr. T. Yamamoto and Prof. S. Matsumura (Kyusyu University) for valuable suggestions for STEM-EDS analyses. The AP-XPS measurements were carried out at SPring-8 BL07LSU as joint research in the Synchrotron Radiation Research Organization and The Institute for Solid State Physics, The University of Tokyo (Proposal No. 2017B7401).

Notes and references

- 1 A. Trovarelli, P. Fornasiero, Eds. *Catalysis by Ceria and Related Materials*; Imperial College Press, London, 2013.
- 2 T. Montini, M. Melchionna, M. Monai, P. Fornasiero, *Chem. Rev.* 2016, **116**, 5987-6041.
- 3 P. Li, X. Chen, Y. Li, J. W. Schwank, *Catal. Today* 2019, **327**, 90-115.
- 4 E. Aneggi, M. Boaro, C. de Leithenburg, G. Dolcetti, A. Trovarelli, *J. Alloys Comp.* 2006, **408-412**, 1096-1102.
- 5 E. W. McFarland, H. Metiu, *Chem. Rev.* 2013, **113**, 4391-4427.
- 6 M. Boaro, M. Vicario, C. de Leithenburg, G. Dolcetti, A. Trovarelli, *Catal. Today* 2003, **77**, 407-417.
- 7 M. Ozawa, M. Kimura, A. Isogai, *J. Alloys Comp.* 1993, **193**, 73-75.
- 8 A. Morikawa, K. Kikuta, A. Suda, H. Shinjo, *App. Catal. B Environ.*, 2009, **88**, 542-549.
- 9 P. G. Harrison, I. K. Ball, W. Azelee, W. Daniell, D. Goldfarb, *Chem. Mater.* 2000, **12**, 3715-3725.
- 10 B. Murugan, A. V. Ramaswamy, D. Srinivas, C. C. Gopinath, V. Ramaswamy, *Chem. Mater.* 2005, **17**, 3983-3993.
- 11 A. Gomez-Cortes, Y. Marquez, J. Arenas-Alatorre, G. Diaz, *Catal. Today* 2008, **133-135**, 743-749.
- 12 P. Singh, M. S. Hegde, J. Gopalakrishnan, *Chem. Mater.* 2008, **20**, 7268-7273.
- 13 J. Beckers, G. Rothenberg, *Dalton Trans*, 2008, 6573-6578.
- 14 C. Liang, Z. Ma, H. Lin, L. Ding, J. Qiu, W. Frandsen, D. Su, *J. Mater. Chem.* 2009, **19**, 1417-1424.
- 15 P. Singh, M. S. Hegde, *Chem. Mater.* 2010, **22**, 762-768.
- 16 X. Yao, C. Tang, Z. Ji, Y. Dai, Y. Cao, F. Gao, L. Dong, Y. Chen, *Catal. Sci. Tech.* 2013, **3**, 688-698.
- 17 Y. Li, Z. Wei, J. Sun, F. Gao, C. H. F. Peden, Y. Wang, *J. Phys. Chem. C* 2013, **117**, 5722-5729.
- 18 I. Moog, C. Prestipino, S. Figueroa, J. Majimel, A. Demourgues, *J. Phys. Chem. C* 2014, **118**, 22746-22753.
- 19 P. Zhang, H. Lu, Y. Zhou, L. Zhang, Z. Wu, S. Yang, H. Shi, Q. Zhu, Y. Chen, S. Dai, *Nat. Commun.* 2015, **6**, 8446.
- 20 M. Konsolakis, M. Sgourakis, S. A. C. Carabiniro, *App. Surf. Sci.* 2015, **341**, 48-54.
- 21 D. Jampaiah, S. J. Ippolito, Y. M. Sabri, B. M. Reddy, S. K. Bhargava, *Catal. Sci. Tech.* 2015, **5**, 2913-2924.
- 22 M. Konsolakis, S.A. C. Carabiniro, E. Papista, G. E. Marnellos, P. B. Tavares, J. Agostinho Moreira, Y. Romaguera-Barcelay, J. L. Figueiredo, *Catal. Sci. Tech.* 2015, **5**, 3714-3727.
- 23 C. Deng, M. Li, J. Qian, Q. Hu, M. Huang, Q. Lin, Y. L. Ruan, Dong, B. Li, M. Fan, *Chem. Asian J.* 2016, **11**, 2144-2156.
- 24 A. Davo-Quinonero, M. Navlani-Garcia, D. Lozano-Castello, A. Bueno-Lopez, J. A. Anderson, *ACS Catal.* 2016, **6**, 1723-1731.
- 25 R. O. Fuentes, L. M. Acuna, C. A. Leyva, N. Sousa, F. M. Figueiredo, *RSC Adv.* 2016, **6**, 64861-64870.
- 26 D. Jampaiah, P. Venkataswamy, V. Elizabeth Coyle, B. M. Reddy, S. K. Bhargava, *RSC Adv.* 2016, **6**, 80541-80548.
- 27 K. J. Lee, Y. Kim, J. H. Lee, S. J. Cho, J. H. Kwak, H. R. Moon, *Chem. Mater.* 2017, **29**, 2874-2882.
- 28 Y. Xiong, L. Li, Lei, Zhang, Y. Cao, S. Yu, C. Tang, L. Dong, *Phys. Chem. Chem. Phys.* 2017, **19**, 21840-21847.
- 29 D. Li, K. Li, R. Xu, H. Wang, D. Tian, Y. Wei, X. Zhu, C. Zeng, L. Zeng, *Catal. Today* 2018, **318**, 73-85.
- 30 Z. Li, X. Guo, F. Tao, R. Zhou, *RSC Adv.* 2018, **8**, 25283-25291.
- 31 P. Sudarsanam, B. Hillary, M. H. Amin, N. Rockstroh, U. Bentrup, A. Bruckner, S. K. Bhargava, *Langmuir* 2018, **34**, 2663-2673.
- 32 J. Lu, J. Wang, Q. Zou, D. He, L. Zhang, Z. Xu, S. He, Y. Luo, *ACS Catal.* 2019, **9**, 2177-2195.
- 33 Z. Liu, J. Li, M. Buettner, R. V. Ranganathan, M. Uddi, R. Wang, *ACS Appl. Mater. Interfaces* 2019, **11**, 17035-17049.
- 34 D. Li, K. Li, R. Xu, X. Zhu, Y. Wei, D. Tian, X. Cheng, H. Wang, *ACS Appl. Mater. Interfaces* 2019, **11**, 19227-19241.
- 35 M. S. Hegde, G. Madras, K. C. Patil, *Acc. Chem. Res.* 2009, **42**, 704-712.
- 36 P. Bera, M. S. Hegde, *RSC Adv.* 2015, **5**, 94949-94979.
- 37 M. S. Hedge, P. Bera, *Catal. Today* 2015, **253**, 40-50.
- 38 J. El Fallah, S. Boujana, H. Dexpert, A. Kiennemann, J. Majerus, O. Touret, F. Villain, F. Le Normand, *J. Phys. Chem.* 1994, **98**, 5522-5533.
- 39 A. Gayen, K. R. priolkar, P. R. Sarode, V. Jayaram, M. S. Hegde, G. N. Subbanna, S. Emura, *Chem. Mater.* 2004, **11**, 2317-2328.
- 40 T. Miyazawa, K. Okumura, K. Kunimori, K. Tomishige, *J. Phys. Chem. B*, 2008, **112**, 2574-2583.
- 41 P. Singh, M. S. Hegde, *Chem. Mater.* 2009, **21**, 3337-3345.
- 42 S. Parres-Esclapez, M. J. Illan-Gmez, C. S. Salinas-Martinez de Lecea, A. Bueno-Lopez, *App. Cat. B Environ.*, 2010, **96**, 370-378.
- 43 M. Kurnatowska, L. Kepinski, *Mater. Res. Bull.*, 2013, **48**, 852-862.
- 44 Y. Zhu, S. Zhang, J. Shan, L. Nguyen, S. Zhan, X. Gu, F. Tao, *ACS Catal.* 2013, **3**, 2627-2369.
- 45 K. Sato, K. Adachi, Y. Takita, K. Nagaoka, *ChemCatChem*, 2014, **6**, 784-789.
- 46 M. Kurnatowaska, M. Schuster, W. Mista, W. L. Kepinski, *ChemCatChem*, 2014, **6**, 3125-3134.
- 47 N. C. Nelson, J. S. Manzano, A. D. Sadow, S. H. Overbury, I. I. Slowing, *ACS Catal.* 2015, **5**, 2051-2061.
- 48 C. I. Hiley, J. M. Fisher, D. Thompsett, R. J. Kashtiban, J. Sloan, R. I. Walton, *J. Mater. Chem. A* 2015, **3**, 13072-13079.
- 49 K. Sevcikova, V. Nehasil, M. Vorokhta, S. Haviar, V. Matolin, I. Matolinova, K. Masek, I. Pis, K. Kobayashi, M. Kobata, T. Nagata, Y. Matsushita, H. Yoshikawa, *Mater. Res. Bull.* 2015, **67**, 5-13.
- 50 E. Varga, P. Pusztai, A. Oszko, K. Baan, A. Erdohelyi, Z. Konya, J. Kiss, *Langmuir* 2016, **32**, 2761-2770.
- 51 K. Sevikova, L. Szabova, M. Kettner, P. Homola, N. Tsud, S. Fabris, V. Matolin, V. Nehasil, *J. Phys. Chem. C*, 2016, **120**, 5468-5476.

- 52 L. S. Kibis, T. Y. Kardash, E. A. Derevyannikova, O. A. Stonkus, E. M. Slavinskaya, V. S. Svetlichnyi, A. I. Boronin, *J. Phys. Chem. C* 2017, **121**, 26925-26938.
- 53 Y. Guo, S. Mei, K. Yuan, D.-J. Wang, H.-C. Liu, C.-H. Yan, Y.-W. Zhang, *ACS Catal.* 2018, **8**, 6203-6215.
- 54 E. A. Derevyannikova, T. Y. Kardash, A. I. Stadnichenko, O. A. Stonkus, E. M. Slavinskaya, V. S. Svetlichnyi, A. I. Boronin, *J. Am. Chem. Soc.* 2018, **140**, 9558-9565.
- 55 P. Fornasiero, R. Di Monte, G. Ranga Rao, J. Kasper, S. Meraiani, A. Trovarelli, M. Graziani, *J. Catal.* 1995, **151**, 168-177.
- 56 F. Fajardie, J.-F. Tempere, J.-M. Manoli, O. Touret, G. Blanchard, G. Djega-Mariadassou, *J. Catal.* 1998, **179**, 469-476.
- 57 P. Fornasiero, J. Kaspar, V. Sergo, M. Graziani, *J. Catal.* 1999, **182**, 56-69.
- 58 C. E. Holi, A. Brenner, K. Y. S. Ng, K. M. Rahmoeller, D. Belton, *Catal. Today* 1999, **50**, 299-308.
- 59 G. Vlaic, R. Di Monte, P. Fornasiero, E. Fonda, J. Kaspar, M. Graziani, *J. Catal.* 1999, **182**, 378-389.
- 60 T. Baidya, A. Gayen, M. S. Hedge, N. Ravishankar, L. Dupont, *J. Phys. Chem. B* 2006, **110**, 5262-5272.
- 61 T. Yamamoto, A. Suzuki, Y. Nagai, T. Tanabe, F. Dong, Y. Inada, M. Nomura, M. Tada, Y. Iwasawa, *Angew. Chem. Int. Ed.*, 2007, **46**, 9253-9256.
- 62 M. Haneda, K. Shinoda, A. Nagane, O. Houshito, H. Takagi, Y. Nakahara, K. Hiroe, T. Fujitani, H. Hamada, *J. Catal.* 2008, **259**, 223-231.
- 63 A. Gupta, A. Kumar, U. V. Waghmare, M. S. Hegde, *Chem. Mater.* 2009, **21**, 4880-4891.
- 64 A. Gupta, M. S. Hegde, K. R. Priolkar, U. V. Waghmare, P. R. Sarode, S. Emura, *Chem. Mater.* 2009, **21**, 5836-5847.
- 65 Gupta, A.; Waghmare, U. V.; Hegde, M. S. *Chem. Mater.* 2010, **22**, 5184-5198.
- 66 P. Singh, M. S. Hegde, *Dalton Trans.* 2010, **39**, 10768-10780.
- 67 Q. Wang, G. Li, B. Zhao, M. Shen, R. Zhou, *App. Catal. B Environ.* 2010, **101**, 150-159.
- 68 M. Tada, S. Zhang, S. Malwadkar, N. Ishiguro, J. Soga, Y. Nagai, K. Tezuka, H. Imoto, S. Otsuka-Yao-Matsuo, S. Ohkoshi, Y. Iwasawa, *Angew. Chem. Int. Ed.* 2012, **51**, 9361-9365.
- 69 S. Mandal, C. Santra, K. K. Bando, O. O. James, S. Maity, D. Mehta, B. Chowdhury, *J. Mol. Catal. A Chem.* **2013**, **378**, 47-56.
- 70 V. M. Shinde, G. Madras, *App. Catal. B Environ.*, 2013, **138-139**, 51-61.
- 71 P. Topka, R. Delaigle, L. Kaluza, E. M. Gaigneaux, *Catal. Today*, **2015**, **253**, 172-177.
- 72 T. Cwele, N. Madadevaiah, S. Singh, H. B. Friedrich, A. K. Yadav, S. N. Jha, D. Bhattacharyya, N. K. Sahoo, *Catal. Sci. Tech.* 2016, **6**, 8104-8116.
- 73 Y. Cao, R. Ran, X. Wu, X. Wu, J. Wan, D. Weng, *Catal. Today*. 2017, **281**, 490-499.
- 74 L. Yang, X. You, Z. Sheng, D. Ma, D. Yu, X. Xiao, S. Wang, *New, J. Chem.* 2018, **42**, 11673-11681.
- 75 S. Li, S. Yan, Y. Xia, B. Cui, Y. Pu, Y. Ye, D. Wang, Y.-Q. Liu, B. Chen, *App. Catal. A General*, 2019, **570**, 299-307.
- 76 S.-J. Hwang, J.-Ho, Choi, *J. Phys. Chem. B*. 2003, **107**, 5791-5796.
- 77 A. Pantelouris, H. Modorow, M. Pantelouris, J. Hormes, D. Reinen, *Chem. Phys.* 2004, **300**, 13-22.
- 78 M. C. Biesinger, C. Brown, J. R. Mycroft, R. D. Davidson, N. S. McIntyre, *Surf. Int. Anal.* 2004, **36**, 1550.
- 79 M. Aronniemi, J. Sainio, J. Lahtinen, *Surf. Sci.* 2005, **578**, 108-123.
- 80 Y. Abe, K. Kato, M. Kawamura, K. Sasaki, *Surf. Sci. Spec.* 2001, **8**, 117-125.
- 81 A. Bianconi, M. Marcelli, H. Dexpert, R. Karnatak, A. Kotani, T. Jo, J. Petiau, *Phys. Rev. B* 1987, **35**, 806-812.
- 82 D. R. Mullins, *Surf. Sci. Rep.*, 2015, **70**, 42-85.
- 83 F. Zhang, Q. Jin, S.-W. Chan, *J. Appl. Phys.*, 2004, **95**, 4319-4326.
- 84 K. Zhou, X. Wang, X. Sun, Q. Peng, Y. Li, *J. Catal.* 2005, **229**, 206-212.
- 85 Ravel B.; Newville, M. *J. Synchrotron Rad.* **2005**, **12**, 537-541.
- 86 Newville, M.; Ravel, B.; Haskel, D.; Rehr, J. J.; Stern, E. A.; Yacoby, Y. *Physica B* **1995**, **208-209**, 154-156.
- 87 Bearden, J. A.; Burr, A. F. *Rev. Mod. Phys.* **1967**, **39**, 125-142.
- 88 Newville, M. *J. Synchrotron Rad.* **2001**, **8**, 322-324.
- 89 Newville, M.; Livinš, P.; Yacoby, Y.; Rehr, J. J.; Stern, E. A. *Phys. Rev. B* **1993**, **47**, 14126-14131.

TOC graphics

Low-Temperature Redox-Active Cr and Rh-Incorporated Ceria Catalyst

The low-temperature redox activity on Cr and Rh-incorporated ceria catalyst was derived from the concerted activation of all three metal species.